

Covariant Jacobi-Legendre expansion for total energy calculations within the projector-augmented-wave formalism

Bruno Focassio^{1, *} Michelangelo Domina^{1,2} Urvesh Patil^{1,2} Adalberto Fazzio^{1,3,4} and Stefano Sanvito^{1,2,†}

¹ Brazilian Nanotechnology National Laboratory (LNNano/CNPEM), 13083-100, Campinas, SP, Brazil

² School of Physics and CRANN Institute, Trinity College Dublin, Dublin 2, Ireland

³ Ilum School of Science, CNPEM, 13083-970 Campinas, São Paulo, Brazil

⁴ Federal University of ABC (UFABC), 09210-580 Santo André, São Paulo, Brazil

(Dated: October 3, 2024)

Machine-learning models can be trained to predict the converged electron charge density of a density functional theory (DFT) calculation. In general, the value of the density at a given point in space is invariant under global translations and rotations having that point as a center. Hence, one can construct locally invariant machine-learning density predictors. However, the widely used projector augmented wave (PAW) implementation of DFT requires the evaluation of the one-center augmentation contributions, that are not rotationally invariant. Building on our recently proposed Jacobi-Legendre charge-density scheme, we construct a covariant Jacobi-Legendre model capable of predicting the local occupancies needed to compose the augmentation charge density. Our formalism is then applied to the prediction of the energy barrier for the 1H-to-1T phase transition of two-dimensional MoS₂. With extremely modest training, the model is capable of performing a non-self-consistent nudged elastic band calculation at virtually the same accuracy as a fully DFT-converged one, thus saving thousands of self-consistent DFT steps. Furthermore, at variance with machine-learning force fields, the charge density is here available for any nudged elastic band image, so that we can trace the evolution of the electronic structure across the phase transition.

I. INTRODUCTION

The accurate prediction of material properties is the ultimate goal of computational materials science and one of the key enablers for new materials development. Density functional theory (DFT) [1, 2] is today the most widely used *ab initio* method to compute materials properties. The DFT's success is due, among other reasons, to the very favourable trade-off between accuracy and computational overhead [3], a trade-off that can be fine-tuned to the system of interest by selecting the most appropriate exchange-correlation energy functional [4] and numerical implementation.

The absence of an accurate density functional for the non-interacting kinetic energy restricts the direct minimization of the DFT energy to the solution of a set of single-particle equations, known as the Kohn-Sham (KS) equations [2]. These enter an iterative process, known as the self-consistent field (SCF) method, where at convergence the charge density defining the single-particle potential must equal that computed by solving the KS equations. Such self-consistent procedure constitutes the main numerical overhead of a DFT calculation. Any effort aiming at reducing the number of steps in a self-consistent cycle, or eliminating them completely, will enable a significant computational speed up and consequently will enhance the throughput. Machine learning (ML) may represent a possible avenue for reaching such a goal.

In recent years, ML has become an important tool in computational materials science, with applications distributed over a wide range of tasks [5]. ML force fields [6] are DFT-accurate energy models enabling large-scale task farming such as those needed in molecular dynamics simulations [7–9], crystal structure prediction [10, 11] or convex-hull-diagram construction [12–16]. Alternatively, ML models can be constructed on either experimental or theoretical data, or on a combination of both, to enable rapid materials screening and the formulation of generative algorithms [17–20]. Most importantly for this discussion, ML has been used to augment the development of DFT itself [21]. The numerical construction of quantum-chemistry-accurate DFT functionals for specific materials [22–25] and for model Hamiltonian [26–29], are just two examples.

Importantly, as the Hohenberg-Kohn theorem [1] establishes a one-to-one correspondence between the electron charge density and the external potential, it is clear that the knowledge of the atomic structure, determining the potential, should be sufficient to obtain the density. This means that, in principle, one can define a ML model that uses structural information to construct the DFT charge density. Such models can then be implemented for approximated exchange-correlation functionals, since the necessary training set can be generated by running standard DFT calculations. Several of such ML charge density models have been proposed, where either a local-orbital [30–33] or a real-space [34–37] representation of the charge density is used together with various ML algorithms. Once the converged ground-state charge density is generated, the associated observables (e.g. the dipole moment of a molecule) can be computed either directly [38, 39] or through additional ML models using the

* bruno.focassio@lnnano.cn pem.br

† sanvitos@tcd.ie

density as an input [40]. A second possibility is to use the ML-computed charge density as the initial density of a new Kohn-Sham self-consistent cycle. For an extremely accurate density, no further self-consistency will be needed and all the quantities available from KS-DFT will be computed without any further numerical effort, except for a single-shot solution of the Kohn-Sham equations. Otherwise, even for non-ultra-accurate ML models, one can still expect the ML density to be a convenient starting point of a reduced self-consistent cycle. In both cases, the ML construction of the charge density can be integrated as an accelerator in any standard theoretical study involving DFT.

Based on our Jacobi-Legendre (JL) cluster expansion for machine-learning force fields [41], we have recently developed an efficient scheme to construct the DFT ground-state charge density over a real space grid [37]. This predicts highly accurate charge densities, while demanding an extremely limited number of DFT calculations to perform the training. Most importantly, the model is constructed over an intrinsic many-body representation (the JL expansion), whose accuracy and complexity can be systematically tuned, but it is linear and thus lean. This means that the computational overheads for both training and inference remain very competitive and a parallel implementation is trivial. Although such JL charge density model can be implemented with any DFT code writing the electron density over a real-space grid, it is currently implemented for the valence density obtained by the VASP package [42, 43]. This uses the projector augmented wave (PAW) formalism, which is an efficient method to deal with the rapidly varying wavefunctions close to the atomic nuclei [44, 45], and it is implemented in a multitude of DFT packages [42, 43, 46–49].

In the PAW scheme, the total all electron wavefunction is written as a sum of two components, one that can be represented over a sparse Fourier/real-space grid and the other that is expanded over a dense atom-centered real-space grid close to the nuclei. These separated components are not independent from each other and are updated simultaneously during the SCF iterations. The separation in the wavefunction is also inherited by the charge density, so that both components are needed to construct the density-dependent Hamiltonian. In particular, in the PAW scheme it is convenient to work with the charge-compensated density, whose atom-centered component is completely determined by the PAW augmentation occupancies [45]. These are, therefore, essential to restart a VASP calculation. Hence, an ML model predicting the total density, then capable of being integrated with a PAW DFT workflow, should provide both the real-space charge-density component and the PAW occupancies.

This work generalizes our JL charge-density model [37] to the prediction of the PAW occupancies. The main difference is that, while the charge density at a point in space is invariant for rotations of the local chemical environment about that point, the PAW occupancy is only

covariant. Hence, here we first provide a general formulation of a covariant JL cluster expansion (Section II A), and then we show how this can be used for predicting the PAW occupancies (Section II B). The method is then applied to the calculation of the transition barrier between the 1H and 1T phases of MoS₂. After training over a very limited number of DFT calculations (Section III A), we will show that a combined JL charge-density and JL PAW occupancies model enable non-self-consistent nudged-elastic-band simulations at the same accuracy of fully converged ones, but at a tiny fraction of the computational costs (Section III B). Finally, we will provide some conclusions and an outlook on the potential of our scheme for materials design (Section IV). The paper is then complemented by three appendices, providing details of the DFT calculations, information about the hyperparameters optimization, and a pointer to our datasets.

II. METHODS

A. Covariant Jacobi-Legendre cluster expansion

The formalism that we will develop here takes directly from our recently formulated Jacobi-Legendre potential (JLP) [41] and Jacobi-Legendre charge-density model (JLCDM) [37]. In those two cases, the cluster expansion was constructed for quantities, the atomic energy and the charge density at a grid point, invariant for rotations of the chemical environment with respect to the point of interest. Here such class of models is generalized to covariant quantities, and we call the new formalism covariant Jacobi-Legendre (CJL) cluster expansion. Consider a target quantity, T_i , associated with the i -th atom in the system. This can be generally written as a many-body expansion,

$$T_i(\hat{\mathbf{r}}_{gi}) = T_i^{(1B)}(\hat{\mathbf{r}}_{gi}) + T_i^{(2B)}(\hat{\mathbf{r}}_{gi}) + T_i^{(3B)}(\hat{\mathbf{r}}_{gi}) + \dots, \quad (1)$$

where the superscripts represent the body order of the expansion, while the index i labels the atoms. Here, $\hat{\mathbf{r}}_{gi}$ is the versor along the direction connecting the i -th atom and the point g in Cartesian space. Thus, as with the LCDM, T_i is expanded over a Cartesian space mapped onto a real-space grid, but now the quantity of interest is localized at the atomic positions.

The various terms in the expansion can be explicitly

written as

$$T_i^{(1B)}(\hat{\mathbf{r}}_{gi}) = a_0^{Z_i}, \quad (2)$$

$$T_i^{(2B)}(\hat{\mathbf{r}}_{gi}) = \sum_{j \neq i} \sum_{nl} a_{nl}^{Z_j Z_i} \bar{P}_{nji}^{(\alpha, \beta)} P_l^{gji}, \quad (3)$$

$$T_i^{(3B)}(\hat{\mathbf{r}}_{gi}) = \sum_{(j,k)_i}^{\text{unique}} \sum_{\substack{n_1 n_2 \\ l_1 l_2 l_3}} a_{n_1 n_2}^{Z_j Z_k Z_i} \times \sum_{\text{symm}} \left(\bar{P}_{n_1 ji}^{(\alpha, \beta)} \bar{P}_{n_2 ki}^{(\alpha, \beta)} P_{l_1}^{gji} P_{l_2}^{gki} P_{l_3}^{jki} \right). \quad (4)$$

In the equations (2), (3) and (4), we have used the vanishing Jacobi polynomials, $\tilde{P}_{nji}^{(\alpha, \beta)}$, defined as

$$\tilde{P}_{nji} = \begin{cases} P_n(x_{ji}) - P_n(-1) & \text{for } -1 \leq x_{ji} \leq 1 \\ 0 & \text{for } x_{ji} < -1 \end{cases} \quad (5)$$

and the double-vanishing-Jacobi polynomials, $\bar{P}_{nji}^{(\alpha, \beta)}$, defined as

$$\bar{P}_{nji} = \tilde{P}_n(x_{ji}) - \frac{\tilde{P}_n(1)}{\tilde{P}_1(1)} \tilde{P}_1(x_{ji}) \quad \text{for } n \geq 2, \quad (6)$$

where for simplicity of notation we have omitted the parameters α and β , which define the specific shape of the Jacobi polynomials of order n , $P_n^{(\alpha, \beta)}$. In the expression above we have also introduced $x_{ji} = \cos\left(\pi \frac{r_{ji} - r_{\min}}{r_{\text{cut}} - r_{\min}}\right)$, with r_{\min} and r_{cut} the minimum and cutoff radius, respectively, and the Legendre polynomial $P_l^{gji} = P_l(\hat{\mathbf{r}}_{gi} \cdot \hat{\mathbf{r}}_{ji})$. Note that up to the two-body order term, $T_i^{(2B)}$, no symmetries must be explicitly included, since the central atom is distinct from the others. Then, for the three-body term, $T_i^{(3B)}$, symmetries are relative only to the exchange of the atoms j and k .

In general, a given function can be written over its harmonics components as

$$f(\hat{\mathbf{r}}) = \sum_{lm} f_{lm} Y_{lm}(\hat{\mathbf{r}}), \quad (7)$$

where we have assumed that $f(\hat{\mathbf{r}})$ is real so that an expansion over real spherical harmonics, $Y_{lm}(\hat{\mathbf{r}})$, will return real radial components, f_{lm} . This assumption is not necessary and can be released by taking complex coefficients or complex spherical harmonics. The expansion coefficients are evaluated as,

$$f_{lm} = \int f(\hat{\mathbf{r}}) Y_{lm}(\hat{\mathbf{r}}) d\hat{\mathbf{r}}, \quad (8)$$

namely by projecting over the required angular momentum. Note that the integral in Eq. (8) is over the solid angle spanned by the versor $\hat{\mathbf{r}}$. Let us now apply to our function of interest, $T_i(\hat{\mathbf{r}}_{gi})$, the same expansion, whose radial components can be computed by projection,

$$T_{i,lm} = \int T_i(\hat{\mathbf{r}}_{gi}) Y_{lm}(\hat{\mathbf{r}}_{gi}) d\hat{\mathbf{r}}_{gi}. \quad (9)$$

The linearity of the expansion in Eq. (1) establishes that the coefficients $T_{i,lm}$ can be written as the sum of different body-order contributions.

For the 1-body term, $T_{i,lm}^{(1B)}(\hat{\mathbf{r}}_{gi})$, using Eq. (2), the angular integrals all vanish, except that for $l = 0$,

$$T_{i,lm}^{(1B)} = \int T_i^{(1B)}(\hat{\mathbf{r}}_{gi}) Y_{lm}(\hat{\mathbf{r}}_{gi}) d\hat{\mathbf{r}}_{gi} = \delta_{l0} \delta_{m0} \sqrt{4\pi} a_0^{Z_i}. \quad (10)$$

This corresponds to a contribution that arises only in the scalar (spherically symmetric) scenario.

In order to evaluate the 2-body term, $T_{i,lm}^{(2B)}$, we consider the addition theorem for spherical harmonics (decomposition of a Legendre polynomial over spherical harmonics), which reads

$$P_l^{gji} = \frac{4\pi}{2l+1} \sum_m Y_{lm}(\hat{\mathbf{r}}_{gi}) Y_{lm}(\hat{\mathbf{r}}_{ji}). \quad (11)$$

Then, by using the orthogonality condition,

$$\int Y_{lm}(\hat{\mathbf{r}}_{gi}) Y_{l'm'}(\hat{\mathbf{r}}_{gi}) d\hat{\mathbf{r}}_{gi} = \delta_{ll'} \delta_{mm'}, \quad (12)$$

we obtain

$$T_{i,lm}^{(2B)} = \int T_i^{(2B)}(\hat{\mathbf{r}}_{gi}) Y_{lm}(\hat{\mathbf{r}}_{gi}) d\hat{\mathbf{r}}_{gi} = \frac{4\pi}{2l+1} \sum_{j \neq i} \sum_n a_{nl}^{Z_j Z_i} \bar{P}_{nji}^{(\alpha, \beta)} Y_{lm}(\hat{\mathbf{r}}_{ji}). \quad (13)$$

Note that this term is fully covariant, since, under rotations, it follows the same transformation rules of the spherical harmonics.

Finally, the 3-body term, $T_{i,lm}^{(3B)}$, is evaluated in a similar way, by expanding the Legendre polynomials that depend on the grid point with the spherical-harmonics addition theorem. One can then perform the integration

$$\int Y_{l_1 m_1}(\hat{\mathbf{r}}_{gi}) Y_{l_2 m_2}(\hat{\mathbf{r}}_{gi}) Y_{lm}(\hat{\mathbf{r}}_{gi}) d\hat{\mathbf{r}}_{gi} = {}^R G_{m_1 m_2 m}^{l_1 l_2 l}, \quad (14)$$

where we have used the real Gaunt symbols, ${}^R G_{m_1 m_2 m}^{l_1 l_2 l}$. Thus, we obtain

$$T_{i,lm}^{(3B)} = \int T_i^{(3B)}(\hat{\mathbf{r}}_{gi}) Y_{lm}(\hat{\mathbf{r}}_{gi}) d\hat{\mathbf{r}}_{gi} = \sum_{(j,k)_i}^{\text{unique}} \sum_{\substack{n_1 n_2 \\ l_1 l_2 l_3}} \frac{(4\pi)^2}{(2l_1+1)(2l_2+1)} a_{n_1 n_2}^{Z_j Z_k Z_i} \times \sum_{\text{symm}} \left(\bar{P}_{n_1 ji}^{(\alpha, \beta)} \bar{P}_{n_2 ki}^{(\alpha, \beta)} P_{l_3}^{jki} \times \sum_{m_1 m_2} {}^R G_{m_1 m_2 m}^{l_1 l_2 l} Y_{l_1 m_1}(\hat{\mathbf{r}}_{ji}) Y_{l_2 m_2}(\hat{\mathbf{r}}_{ki}) \right), \quad (15)$$

where the second sum runs over the unique indexes n_1 , n_2 , taking care that the coefficient $a_{n_1 n_2}^{Z_j Z_k Z_i}$ is invariant $l_1 l_2 l_3$

under the simultaneous exchange of the species indexes $Z_j \leftrightarrow Z_k$ and the Jacobi indexes $n_1 \leftrightarrow n_2$, and therefore runs over non-equivalent coefficients ($n_1 \geq n_2$). The third sum takes care of the symmetries (symm) by manually evaluating cases with equivalent coefficients with respect to $n_1 \leftrightarrow n_2$. More details on the symmetries of the coefficients can be found in Ref. [41]. We remark here that the pre-factor of the expansion coefficients, $a_{n_1 n_2}^{Z_j Z_k Z_i}$, is not affected by the symmetrization operation, since this involves the simultaneous exchange of the indexes $n_1 \leftrightarrow n_2$ and $l_1 \leftrightarrow l_2$, which leaves $T_{i,lm}^{(3B)}$ unaffected.

This procedure creates a recipe to compute the harmonic components for any order of the expansion. The final result for the lm harmonic component of the function T_i is given by the sum of all the terms obtained, namely

$$T_{i,lm} = T_{i,lm}^{(1B)} + T_{i,lm}^{(2B)} + T_{i,lm}^{(3B)} + \dots \quad (16)$$

where the 1-, 2- and 3-body components are now defined as,

$$T_{i,lm}^{(1B)} = \delta_{l0} \delta_{m0} \sqrt{4\pi} a_0^{Z_i}, \quad (17)$$

$$T_{i,lm}^{(2B)} = \frac{4\pi}{2l+1} \sum_{j \neq i} \sum_n \left[\delta_{l0} \frac{1}{\sqrt{4\pi}} a_{n0}^{Z_j Z_i} \tilde{P}_{nji}^{(\alpha,\beta)} + (1 - \delta_{l0}) a_{nl}^{Z_j Z_i} \bar{P}_{nji}^{(\alpha,\beta)} Y_{lm}(\hat{\mathbf{r}}_{ji}) \right], \quad (18)$$

$$T_{i,lm}^{(3B)} = \delta_{l0} \sum_{(j,k)_i}^{\text{unique}} \sum_{n_1 n_2 l_1} (4\pi)^2 a_{n_1 n_2 l_1}^{Z_j Z_k Z_i} \times \sum_{\text{symm}} \left(\bar{P}_{n_1 ji}^{(\alpha,\beta)} \bar{P}_{n_2 ki}^{(\alpha,\beta)} P_{l_1}^{jki} \right) + (1 - \delta_{l0}) \sum_{(j,k)_i}^{\text{unique}} \sum_{\substack{n_1 n_2 \\ l_1 l_2 l_3}} \frac{(4\pi)^2}{(2l_1+1)(2l_2+1)} a_{n_1 n_2}^{Z_j Z_k Z_i} \times \sum_{\text{symm}} \left(\bar{P}_{n_1 ji}^{(\alpha,\beta)} \bar{P}_{n_2 ki}^{(\alpha,\beta)} P_{l_3}^{jki} \right) \times \sum_{m_1 m_2} {}^R G_{m_1 m_2}^{l_1 l_2 l} Y_{l_1 m_1}(\hat{\mathbf{r}}_{ji}) Y_{l_2 m_2}(\hat{\mathbf{r}}_{ki}) \right). \quad (19)$$

One should notice that we separate the $l = 0$ and $l > 0$ contributions. Due to the discontinuity of the spherical harmonics at the origin, in $T_{i,lm}^{(2B)}$, for $l = 0$, we use the vanishing Jacobi polynomials, $\tilde{P}_{nji}^{(\alpha,\beta)}$, defined in Eq. (5), while for $l > 0$, we use the double-vanishing Jacobi polynomials, $\bar{P}_{nji}^{(\alpha,\beta)}$, defined in Eq. (6), since these vanish at the origin. In doing so we keep the expansion continuous. In addition, actual implementations of this formalism can redefine the expansion coefficients so to absorb the pre-factors of Eqs. (17), (18) and (19).

B. Application to PAW augmentation charges

Our goal is to reconstruct the augmentation (compensation) charge density, \hat{n} , which is defined as

$$\hat{n}(\mathbf{r}) = \sum_{ij,LM} \rho_{ij} \hat{Q}_{ij}^{LM}, \quad (20)$$

where ρ_{ij} is the occupancy of the augmentation channel (i, j) and \hat{Q}_{ij}^{LM} is the L -dependent compensation charge. We use here the same notation as that in Ref. [45], to distinguish the charge density $n(\mathbf{r})$ and the augmentation charge density $\hat{n}(\mathbf{r})$. Following the same convention, the indexes i and j represent the collection of labels that are required to fully characterize an augmentation channel, as shown below, and in this context they must not be confused with labels for atomic positions. In order to cluster expand the compensation charge of Eq. (20), it is useful to write it with respect to the site μ at position \mathbf{R}_μ ,

$$\hat{n}_\mu(\mathbf{r}) = \sum_{ij,LM} \rho_{ij} q_{ij}^{LM} g_L(|\mathbf{r} - \mathbf{R}_\mu|) Y_{LM}(\widehat{\mathbf{r} - \mathbf{R}_\mu}), \quad (21)$$

where we have used the expansion,

$$\hat{Q}_{ij}^{LM} = q_{ij}^{LM} g_L(|\mathbf{r} - \mathbf{R}_\mu|) Y_{LM}(\widehat{\mathbf{r} - \mathbf{R}_\mu}), \quad (22)$$

with g_L be a linear combination of two spherical Bessel functions [45], while Y_{LM} be spherical harmonics. Here the q_{ij}^{LM} terms act as expansion coefficients of the compensation charge \hat{Q}_{ij}^{LM} , with respect these functions. By writing explicitly the indexes i and j in terms of (k_1, l_1, m_1) and (k_2, l_2, m_2) , respectively, we obtain

$$\hat{n}_\mu(\mathbf{r}) = \sum_{k_1 k_2}^{\text{unique}} \hat{n}_{\mu k_1 k_2}^{LM} g_L(|\mathbf{r} - \mathbf{R}_\mu|) Y_{LM}(\widehat{\mathbf{r} - \mathbf{R}_\mu}), \quad (23)$$

where we have defined

$$\hat{n}_{\mu k_1 k_2}^{LM} = \sum_{\substack{l_1 l_2 \\ m_1 m_2}} \rho_{k_1 l_1 m_1} q_{k_1 l_1 m_1}^{LM}. \quad (24)$$

These are the harmonics components of \hat{n}_μ , belonging to the subspace of angular momentum (L, M) . The specific nature of each term in the product is unessential for the discussion here, and for further details we refer to the PAW formulation contained in reference [45]. In particular, for each choice of pairs (k_1, k_2) , we can design covariant tensor models that fits the (L, M) harmonic components of \hat{n}_μ , namely

$$T_{\mu,LM} \simeq \sum_{\substack{l_1 l_2 \\ m_1 m_2}} \rho_{k_1 l_1 m_1} q_{k_1 l_1 m_1}^{LM}. \quad (25)$$

The general case would require fitting an expression for

$$\hat{n}_{\mu k_1 k_2}^{LM} = T_{\mu,LM}^{(1B)} + T_{\mu,LM}^{(2B)} + T_{\mu,LM}^{(3B)} + \dots, \quad (26)$$

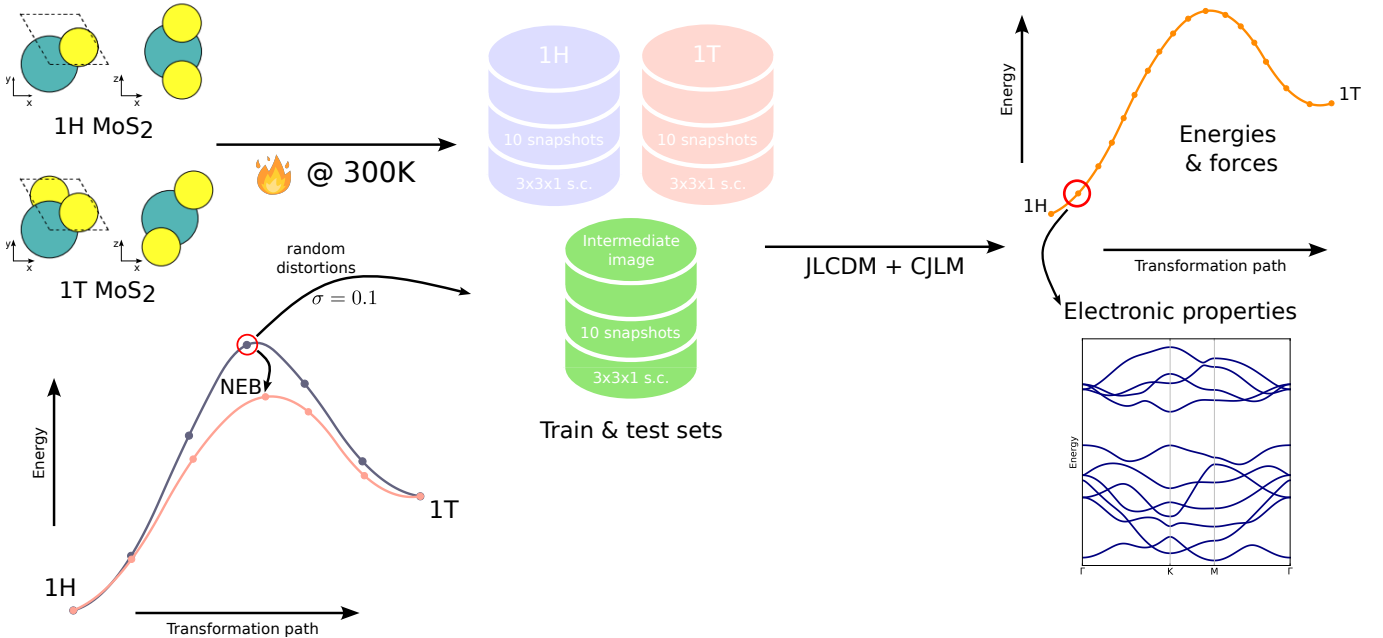


FIG. 1. Illustration of the workflow used to construct a JLCDM and CJL model to predict the converged DFT ground-state charge density and PAW occupancies. Both these ingredients are necessary to start a DFT PAW calculation (with VASP in this case), and here the method is used to predict the energy barrier for the 1H-to-1T structural transition of MoS₂. The creation of the dataset starts by computing the 1H and 1T phase of 2D MoS₂. We perform AIMD at 300 K for each phase and extract 10 snapshots of each, where we take a 1:1 ratio between training and test snapshots. Ten additional data points are created by using random distortions of linearly interpolated structures along the NEB path (before any optimization). This training set is used to construct the JLCD and CJL models, which are then used to predict the charge density and PAW occupancies for any distorted structure with the MoS₂ chemistry. The models can be readily used to predict the entire NEB trajectory and to investigate properties such as the electronic structure along the transition path.

however, we resort to a simplification to reduce the total number coefficients involved in the expansion. Our strategy now is to distinguish three cases. The first case is $l_1 = l_2 = 0$, resulting in $L = M = 0$. For this the appropriate tensor components can be derived directly from Eqs. (17) and (18), restricting this expansion to 1 and 2-body terms,

$$\hat{n}_{\mu 00}^{00} = a_0^{Z_i} + \sum_{j \neq i} \sum_n a_n^{Z_j Z_i} \tilde{P}_{nji}^{(\alpha, \beta)}, \quad (27)$$

where we have incorporated the constant leading factor $\sqrt{4\pi}$ into the a 's coefficients to be fitted. This case is similar to fitting a force field, namely, the component of the augmentation density has spherical symmetry.

Next, we consider the situation where either l_1 or l_2 are zero, but not both. For $l_2 = 0$, we have $l_1 = L \neq 0$. In this case, the quantity of interest is a tensor of order L . Therefore we can write the expression for $\hat{n}_{\mu L 0}^{LM}$ using only the 1-body term as using Eq. (18)

$$\hat{n}_{\mu L 0}^{LM} = \frac{4\pi}{2L + 1} \sum_{j \neq \mu} \sum_n \left[a_n^{Z_j Z_\mu} \bar{P}_{nji}^{(\alpha, \beta)} Y_{LM}(\hat{\mathbf{r}}_{j\mu}) \right]. \quad (28)$$

Finally, we have the most general case where $l_1 \neq l_2 \neq 0$. We can, then, write the harmonic components of the

density using $T_{\mu, l_1, l_2}^{(3B)}$, but without performing the sum over l_1 and l_2 in order to properly account for the angular momentum coupling, namely for $T_{\mu, l_1, l_2}^{(3B)}$ to transform as $n_{\mu l_1, l_2}^{LM}$. Explicitly we have

$$\begin{aligned} n_{\mu l_1, l_2}^{LM} = & \sum_{(j, k)_\mu} \sum_{\substack{\text{unique} \\ l'}}^{} \frac{(4\pi)^2}{(2l_1 + 1)(2l_2 + 1)} a_{n_1 n_2}^{Z_j Z_k Z_\mu} \times \\ & \times \sum_{\text{symm}} \left(\bar{P}_{n_1 j \mu}^{(\alpha, \beta)} \bar{P}_{n_2 k \mu}^{(\alpha, \beta)} P_{l'}^{jk \mu} \times \right. \\ & \left. \times \sum_{m_1 m_2} {}^R G_{m_1 m_2 M}^{l_1 l_2 L} Y_{l_1 m_1}(\hat{\mathbf{r}}_{j\mu}) Y_{l_2 m_2}(\hat{\mathbf{r}}_{k\mu}) \right). \quad (29) \end{aligned}$$

The expressions derived in Eqs. (27) through (29) can now be used to efficiently predict the PAW occupancies. This means that now the training of a JLCDM and a CJL model for the PAW occupancies gives us access to a full machine-learning-predicted charge density. Such density can then be used as a starting point for VASP calculations, and possibly as converged charge density for non-self-consistent DFT.

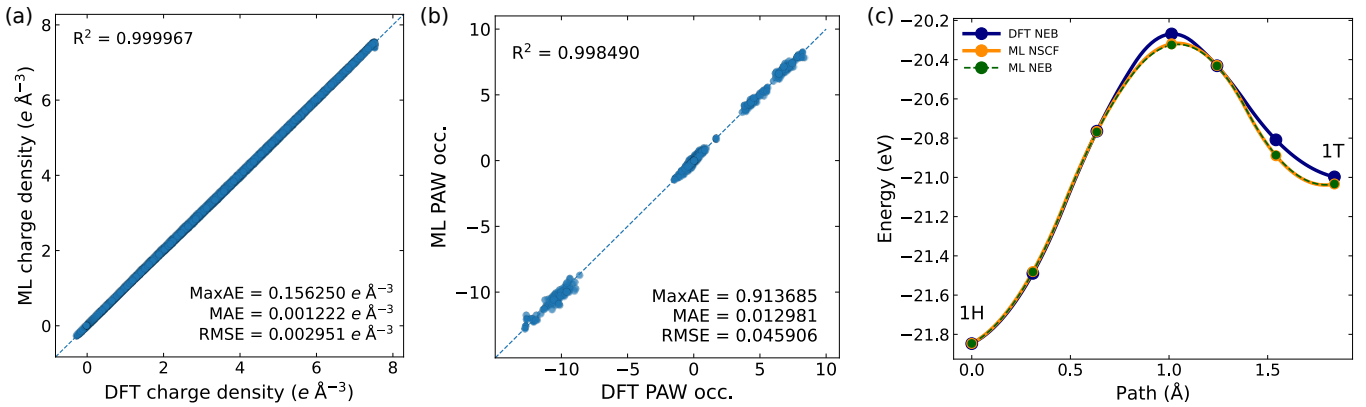


FIG. 2. Parity plots for the various density models constructed for MoS₂, namely (a) the JLCDM and (b) the CJL model. Data are for the test set and the values of the mean absolute error (MAE), root-mean-squared error (RMSE), maximum absolute error (MaxAE), and R^2 metrics are reported. Panel (c) displays the total energy along the transition path between the 1H and 1T phases. The total energy is obtained with NEB calculations using self-consistent DFT total energies and forces (DFT NEB), the ML models at the self-consistent DFT structures (ML NSCF), a fully ML-driven NEB, where the structures are relaxed with non-self-consistent DFT using the ML models (ML NEB). The solid line is a spline interpolation of the actual data (symbols).

III. RESULTS AND DISCUSSION

We now demonstrate the application of the JLCDM together with the CJL model into a typical materials science workflow. In particular, we study the structural transition between the 1H and the 1T phase of 2D MoS₂ monolayer. We will use our machine-learning models to find the transition state and all the desired images along the transition without any self-consistent calculation, but rather, by evaluating non-self-consistently energies and forces. Furthermore, as here energy and forces are obtained from the knowledge of the full electron density, any electronic quantity is also readily available. This is, for instance, the case of the band structure along the transition. Our workflow is illustrated in Fig. 1.

A. Dataset generation and ML models training

Firstly, as in any machine-learning pipeline, we need to generate the data to train the models. The training/test data consists of structures derived from three distinct starting configurations, namely the 1H phase, the 1T phase, and the geometrical midpoint interpolating the atomic Cartesian coordinates of the two phases. For the 1H and 1T phases, we take snapshots from *ab initio* molecular dynamics (AIMD) simulations at 300 K. In contrast, the snapshots of the geometrical midpoint are obtained from random distortions (the standard deviation of the distortion amplitude is 0.1 Å). For each category, we sample 10 distinct geometries and equally split them into training and test data (1:1 ratio), see Fig. 1. The grid point sampling of the valence charge density, described by the JLCDM, is performed with the same procedure established in Ref. [37], a pipeline demonstrated

efficient. Then, the hyperparameter optimization of the JLCDM is carried out through Bayesian optimization using Gaussian Processes over the training set, see Table II in Appendix B for more details. In contrast, when fitting the PAW components, we consider the following l -channels for Mo: 0, 0, 1, 1, 2, 2, and for S: 0, 0, 1, 1. This choice maps all the available components for each atom, following the rule $L = |l_i - l_j|, |l_i - l_j| + 2, \dots, l_i + l_j$, and generates 138 components for the Mo ions and 33 components for the S ions in each snapshot.

In general, the transition state (TS) is computed with the nudged elastic band (NEB) method [50, 51] with climb image [52] as implemented in the ASE package [53]. The energy and the atomic forces needed by the NEB are computed with the VASP code [42, 43]. Conventionally, all DFT calculations are performed self-consistently, but here we will replace those with a non-self-consistent evaluation using our predicted densities. In any case, the starting point of any NEB calculation is the linear interpolation of the initial (1H-MoS₂) and final (1T-MoS₂) structure into intermediate structures, also referred to as images. For our specific problem, we construct 5 images across the transition.

In closing this section we wish to spend a few words on our strategy to generate the models training set. Currently, this is pretty simple, namely we have included a few configurations around the two stable phases and at the geometrical midpoint between them. The question is whether better choices are possible. In general, charge-density models are more subtle to train than machine-learning potentials, since a single DFT calculation generates a large number of training points, in principle all the grid points, but has also significant redundancy. Thus, significant data pruning must be implemented. Then, it is important to note that the final models are typi-

cally rather slim, contain a few thousands of parameters. This means, that simply expanding the number of training configurations, thus expanding the pool of training points, does not guarantee achieving better models. As a consequence, one has to design a strategy to include in the training set the configurations most representative for the problem at hand, effectively an active-learning strategy, here specific of a NEB calculation.

B. Transition-state, energy, and electronic properties

Figure 2 presents the results for the fit of both the JLCDM for the density written over the real-space grid [panel (a)] and the CJL model for the PAW occupancies [panel (b)]. In general, we obtain an extremely accurate JLCDM, with a root-mean-squared error (RMSE) of only $2.9 \cdot 10^{-3} \text{ e}/\text{\AA}^3$, a mean absolute error (MAE) of $1.2 \cdot 10^{-3} \text{ e}/\text{\AA}^3$ and a maximum absolute error (MaxAE) of $0.15 \text{ e}/\text{\AA}^3$. These are a factor 2 to 3 lower than those of our previously published JLCDM for the same compound [37]. Such improvement is related to the slightly expanded training set and to the nature of the test set. In fact, we now train also on interpolated structures along the 1H-1T transition, and not just over the 1H and 1T phases, and we test on different images across the phase transition (in Ref. [37] the test set was formed by distorted images of the 1T' structure).

The same parity plot for the CJL model is presented in Fig. 2(b), again for the test set. Here we aggregate all the PAW components, that is all the (l_i, l_j, L, M) components for all Mo and S atoms. Also in this case the model, which interpolates with only 143 parameters (see Appendix B), returns extremely accurate predictions, with a RMSE of 0.045, a MAE of 0.012 and a MaxAE of 0.91. Thus, the two models combined produce an extremely accurate total charge density that can be readily used to evaluate energy and forces.

Such evaluation is provided in Fig. 2(c), where we present the potential energy surface (PES) across the 1H to 1T transition. In particular, the calculation is performed in three different ways. The ground truth is provided by a fully self-consistent NEB calculation ('DFT NEB', blue line), where each of the images along the path is fully relaxed by using self-consistent DFT with the standard charge-density initialization. Typically, this requires the evaluation of about 1,000 structures in total, so that the computational overheads are that of 1,000 self-consistent DFT calculations. The first test for our ML models is performed over the total energy. For this we take the NEB transition states computed with self-consistent DFT and evaluate their total energy by using the ML density and no self-consistent iteration ('ML NSCF', yellow line). Next, we assess both energy and forces, namely we use the ML models to perform the entire NEB workflow ('ML NEB', green line). In this case, we input the JLCDM-predicted charge density and CJL-

predicted PAW occupations for each structure at each step of the NEB optimization. For these, energy and forces are calculated with non-self-consistent DFT. Thus, in this last part, both the relaxation and the energy evaluation are driven by our charge-density models. This second test is clearly more stringent, since errors may be present in both the energy and the structure evaluation and they can add up. However, should the predictions be valid, one will be able to perform an entirely non-self-consistent PES evaluation, thus saving the computational cost of all the self-consistent iterations involved in the NEB workflow.

In general, we find an excellent agreement between both our ML-driven PES evaluations and the ground truth, with minimal differences associated to the structural evaluation. This means that the ML-driven NEB relaxes at practically the same structures obtained with fully self-consistent DFT, and the remaining error is attributed to the energy of the final structures. More in detail, the models seem to perform better at the 1H side of the PES than at the 1T one. The height of the energy barrier, namely the energy difference between the lowest energy phase (1H) and the transition state, is computed at 1.5270 eV and 1.5212 eV, respectively for ML NSCF and ML NEB, against a self-consistent DFT energy of 1.5783 eV. Thus, the error over the barrier height is 0.0512 eV for ML NSCF and 0.0570 eV for ML NEB. These are errors in the 50 meV range, corresponding to $\sim 3\%$ of the target self-consistent energy-barrier height. The same comparison for the difference in energy between the 1T phase and the transition state energy, returns us 0.7143 eV, 0.7085 eV, and 0.7286 eV, respectively for ML NSCF, ML NEB, and DFT NEB, with a deviation of 0.0142 eV for ML NSCF and of 0.020 eV for ML NEB. These are in the 20 meV range or about 2%. Finally, the difference in energy between the 1H and 1T phase is almost identical for ML NSCF and ML NEB, 0.8127 eV, and again it is extremely close to that computed by self-consistent DFT, 0.8497 eV. See Table I for a summary of the results. With these results at hand, we can conclude that the ML-computed density is certainly sufficient to replace the self-consistent cycle across the entire PES evaluation.

TABLE I. Energies for the transition between the 1H and 1T phase of 2D MoS₂. DFT NEB is the result obtained by the full *ab-initio* NEB calculation. ML NSCF refers to the case, where we compute the energy using ML non-self-consistent DFT at the DFT-relaxed structures. Finally, ML NEB refers to a completely ML-driven NEB (no self-consistent cycles are performed at any point). Here $\Delta E_{\alpha-TS}$ is the absolute energy difference between the α phase and the transition state, while ΔE_{1H-1T} is the absolute energy difference between the two phases.

	ΔE_{1H-1T} (eV)	ΔE_{1H-TS} (eV)	ΔE_{1T-TS} (eV)
DFT NEB	0.8497	1.5783	0.7286
ML NSCF	0.8127	1.5270	0.7143
ML NEB	0.8127	1.5212	0.7085

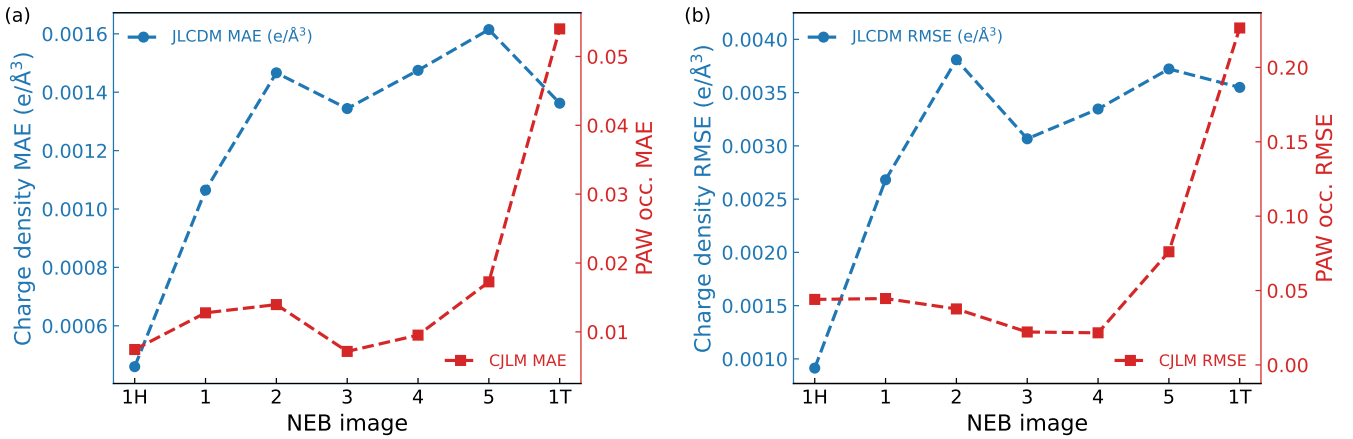


FIG. 3. (a) MAE and (b) RMSE for the two charge-density models computed for each of the NEB images. Note that both density models perform better on the 1H side of the phase transition. However, while the JLCDM away from the 1H phase has similar accuracy for all images, the CJL model has a sharp increase in the error for phases close to the 1T only.

Although small, it is interesting to understand the origin of the deviations between the ML-computed NEB energy and that obtained by self-consistent DFT. This is certainly not attributable to differences in atomic structure that might have resulted from the different relaxation processes. In fact, the energies computed with the ML density at the self-consistent DFT geometries are practically identical to those computed along the ML-NEB curve. Then, the error has to be found in the charge density alone. In order to understand better this point, in Fig. 3 we plot the MAE and RMSE of both charge-density models for all the different NEB images. We find that, the JLCDM performs significantly better for the 1H structure, but then displays a reasonably uniform error across the entire NEB path. For instance, with the exception of the 1H structure the RMSE ranges between $2.6 \cdot 10^{-3}$ $e/\text{\AA}^3$ and $3.7 \cdot 10^{-3}$ $e/\text{\AA}^3$, while the MAE goes from $1.0 \cdot 10^{-3}$ $e/\text{\AA}^3$ to $1.6 \cdot 10^{-3}$ $e/\text{\AA}^3$ (for the 1H structure the RMSE and MAE are $0.9 \cdot 10^{-3}$ $e/\text{\AA}^3$ and $0.4 \cdot 10^{-3}$ $e/\text{\AA}^3$, respectively.) In contrast, the CJL model for the PAW occupancies has a rather constant error across the NEB trajectory, except for the 1T phase and its closest image, where it spikes up. The error increase, in this case, is really significant with both RMSE and MAE of the 1T image being about a factor five larger than their average over the entire structural transition.

The error distribution across the NEB path reflects in the energy error that, as noticed before, is larger on the 1T side of the transition. It is thus clear that, although the models constructed appear already accurate enough to enable an accurate evaluation of the transition barrier, a higher degree of accuracy can be reached by a more balanced training set. In particular, given the fact that the JLCDM and the CJL model are rather different in size, different training sets for the two models may be appropriate.

At variance with ML force fields, the use of the charge density allows one, not only to compute energy and forces

but also any other observable related to the charge density. This is, for instance, the case of the Kohn-Sham spectrum. In other words, we are here able to track the electronic structure of MoS₂ along the 1H-to-1T structural transition. Our results are presented in Figure 4, where we report the band structure and the DOS of the 1H phase, the 1T one, and the structure corresponding to the transition state. In particular, we compare the fully self-consistent DFT electronic structure, with that obtained from the density predicted by our two charge-density models. In general, we find a rather good agreement between the DFT and the ML bands/DOS, an agreement that is certainly much more pronounced at the 1H side of the structural transition. This is a consequence of the better ML-interpolated charge density found for the 1H phase, as already observed in the discussion of the total energy. In any case, the ML models have enough accuracy to predict the insulator-to-metal transition along the structural transformation, with the transition state being already metallic. Interestingly, we find that the accuracy of the ML models is higher in predicting occupied states, with the largest deviation found for bands several eV away from the Fermi level. We also note that the bands computed with the ML density are more accurate at the 1H side of the phase transition, as expected by the error distribution discussed before.

In any case, we can conclude that the ML charge density provides an excellent tool to approximate the electronic structure across structural deformations of a solid/molecule. Here we have considered a rather broad structural ensemble, since it spans across a phase transformation. Should one have a tighter pool of structures, as those sampled in a molecular dynamics simulation at moderate temperature, the agreement will be significantly higher. This will allow us to compute electronic-structure observables (e.g. the band gap or the optical absorption spectrum) at the DFT level, but at the computational cost of non-self-consistent DFT. We believe

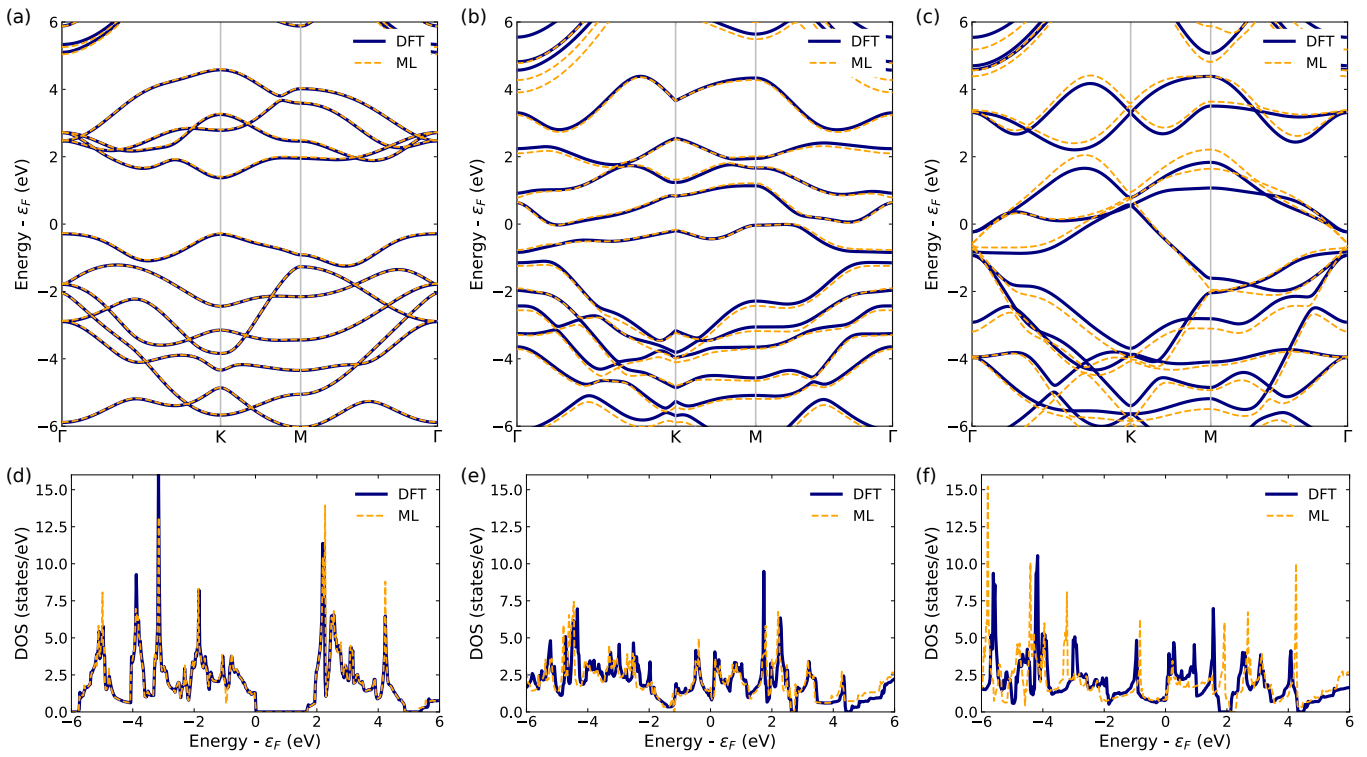


FIG. 4. Band structure and density of states (DOS) for MoS₂ along the 1H-to-1T transition. We compare results obtained from fully self-consistent DFT (black lines) and non-self-consistent DFT with charge density and PAW occupancies obtained from the JL models. Panels (a) and (d) are for 1H, (b) and (e) for the transition state, and (c) and (f) for the 1T phase.

that such an advantage can open the possibility for an inexpensive evaluation of temperature-dependent materials properties from DFT.

IV. CONCLUSION

Extending on our previously introduced JLCDM [37] and JL force field [41], we have here introduced the formalism for an atom-centered covariant Jacobi-Legendre cluster expansion. This is then applied to the prediction of the PAW occupations needed by a PAW-based DFT calculation to represent the full charge density. As such, the covariant cluster expansion together with the JLCDM provides a ML avenue to represent the entire DFT-PAW charge density, that can be used to prepare the starting density of a DFT calculation.

We have implemented such a scheme in the VASP code and tested it for 2D monolayer MoS₂. In particular, we have taken the challenging task of tracking the structural and electronic changes across a transition from the 1H to the 1T phases. This is a rather stringent test, with a significant amount of diversity in the structures to predict. We have found that, with a small training set (only 15 DFT calculations), our ML models were able to reproduce an entire NEB search and to track the electronic structure across the structural transformation. This allows us to save several fully

converged self-consistent DFT calculations. Our results make charge-density models an attractive alternative to machine-learning force fields, since in addition to energy and forces they can reproduce the electronic structure over an ensemble of configurations. Applications related to temperature-dependent properties of materials are thus envisioned.

ACKNOWLEDGMENTS

This work was supported by São Paulo Research Foundation (FAPESP) (Grants no. 2021/12204-6, 2019/04527-0, and 2017/02317-2), and the Irish Research Council Advanced Laureate Award (IRCLA/2019/127). UP thanks additional funding from the Qatar National Research Fund (NPRP12S-0209-190063) and Science Foundation Ireland (19/EPSRC/3605). We acknowledge the DJEI/DES/SFI/HEA Irish Centre for High-End Computing (ICHEC) and Trinity Centre for High Performance Computing (TCHPC) for the provision of computational resources. We acknowledge NVIDIA Academic Hardware Grant Program for providing graphics processing units.

APPENDIX A: DFT CALCULATIONS

All single-point and AIMD calculations are performed using DFT [1, 2] as implemented in the Vienna *ab initio* simulation package (VASP) [42, 43]. The exchange and correlation energy is provided by the generalized gradient approximation (GGA) [54] within the Perdew-Burke-Ernzerhof (PBE) [55] formulation and parameterization. As already discussed, we use projector augmented wave (PAW) [45] pseudopotentials. Single-point self-consistent calculations are performed with a 600 eV kinetic-energy cutoff for the plane-wave expansion, and the Brillouin zone is sampled over a k -point density of $12 / \text{\AA}^{-1}$. AIMD calculations are performed with a 2 fs time-step, and the Nosé-Hoover thermostat [56–58] at 300 K. All AIMD runs are at least 4 ps long, and snapshots are taken from the simulation’s last 3 ps. Random distortions applied to the atomic positions are sampled from a probability distribution using $\sigma = 0.1 \text{ \AA}$ as the standard deviation.

Nudged elastic band (NEB) [50, 51] calculations are performed with climb image [52], as implemented in the ASE package [53]. Energies and forces are calculated using the VASP code, either self-consistently or with the ML charge density and PAW occupations.

From the practical point of view our machine-learning charge density is handled externally from VASP, which has not been modified. In fact, we simply use the tools available in the Pymatgen [59] library to read/write the VASP CHGCAR file. This contains the lattice information and atomic positions, the charge density component on the grid and the augmentation charges. Then, the JL-CDM is used to predict the charge density on the grid and the CJLM to compute the augmentation charges. These are written back on the CHGCAR file by Pymatgen with the correct format.

APPENDIX B: MODEL TRAINING AND HYPERPARAMETERS

The models are fitted by using singular value decomposition to find the pseudo-inverse of the matrix A defin-

ing the equation $A\hat{x} = \hat{b}$ for the coefficients \hat{x} . Training and inference are performed using the Ridge class (with $\alpha = 0$, without fitting an intercept) from the scikit-learn library [60]. The hyperparameters used in the models throughout this work are displayed in Table II. Hyperparameter optimization is performed through Bayesian optimization using Gaussian Processes (`gp_minimize`), as implemented in the scikit-optimize library [61]. This is done solely on part of the training set, where a single snapshot of each phase is used as validation. Using these hyperparameters, we obtain a JLCDM with 1928 features, a model for the \hat{n}_{00}^{00} components with 13 features, a model for the \hat{n}_{LM}^{LM} components with 10 features, and a model for the $\hat{n}_{l_1 l_2}^{LM}$ components with 120 features.

TABLE II. Optimized hyperparameters and corresponding feature size for each of the models generated.

Model	Body	r_{cut}	n_{max}	l_{max}	r_{min}	α	β
JLCDM	1B	4.93	19	-	-0.95	7.35	7.20
	2B	4.93	11	8	0.00	4.28	2.71
CJLM	1B	6.00	6	-	0.00	2.00	2.00
	2B	6.00	6	3	0.00	2.00	2.00
	3B	6.00	4	3	0.00	2.00	2.00

APPENDIX C: DATA AND CODE AVAILABILITY

The data used to train and test the models (DFT charge density, structure files, and trained models) is available via Zenodo [62]. Scripts and related code for calculating the Jacobi-Legendre grid-based linear expansion are available at <https://github.com/StefanoSanvitoGroup/MLdensity>.

[1] P. Hohenberg and W. Kohn, Inhomogeneous Electron Gas, *Phys. Rev.* **136**, B864 (1964).

[2] W. Kohn and L. J. Sham, Self-Consistent Equations Including Exchange and Correlation Effects, *Phys. Rev.* **140**, A1133 (1965).

[3] K. Burke, Perspective on density functional theory, *J. Chem. Phys.* **136**, 150901 (2012).

[4] J. P. Perdew and K. Schmidt, Jacob’s ladder of density functional approximations for the exchange-correlation energy, *AIP Conf. Proc.* **577**, 1 (2001).

[5] H. J. Kulik, T. Hammerschmidt, J. Schmidt, S. Botti, M. A. L. Marques, M. Boley, M. Scheffler, M. Todorović, P. Rinke, C. Osés, A. Smolyanyuk, S. Curtarolo, A. Tkatchenko, A. P. Bartók, S. Manzhos, M. Ihara, T. Carrington, J. Behler, O. Isayev, M. Veit, A. Grisafi, J. Nigam, M. Ceriotti, K. T. Schütt, J. Westermayr, M. Gastegger, R. J. Maurer, B. Kalita, K. Burke, R. Nagaï, R. Akashi, O. Sugino, J. Hermann, F. Noé, S. Pilati, C. Draxl, M. Kuban, S. Rigamonti, M. Scheidgen, M. Ester, D. Hicks, C. Toher, P. V. Balachandran, I. Tamblyn, S. Whitelam, C. Bellinger, and L. M. Ghiringhelli, Roadmap on machine learning in electronic structure, *Electron. Struct.* **4**, 023004 (2022).

[6] O. T. Unke, S. Chmiela, H. E. Sauceda, M. Gastegger, I. Poltavsky, K. T. Schütt, A. Tkatchenko, and K.-R. Müller, Machine Learning Force Fields, *Chem. Rev.* **121**,

10142 (2021).

[7] M. A. Caro, G. Csányi, T. Laurila, and V. L. Deringer, Machine learning driven simulated deposition of carbon films: From low-density to diamondlike amorphous carbon, *Phys. Rev. B* **102**, 174201 (2020).

[8] J. S. Smith, B. Nebgen, N. Mathew, J. Chen, N. Lubbers, L. Burakovsky, S. Tretiak, H. A. Nam, T. Germann, S. Fensin, and K. Barros, Automated discovery of a robust interatomic potential for aluminum, *Nature Commun.* **12**, 1257 (2021).

[9] J. T. Willman, K. Nguyen-Cong, A. S. Williams, A. B. Belonoshko, S. G. Moore, A. P. Thompson, M. A. Wood, and I. I. Oleynik, Machine learning interatomic potential for simulations of carbon at extreme conditions, *Phys. Rev. B* **106**, L180101 (2022).

[10] E. V. Podryabinkin, E. V. Tikhonov, A. V. Shapeev, and A. R. Oganov, Accelerating crystal structure prediction by machine-learning interatomic potentials with active learning, *Phys. Rev. B* **99**, 064114 (2019).

[11] C. J. Pickard, Ephemeral data derived potentials for random structure search, *Phys. Rev. B* **106**, 014102 (2022).

[12] K. Gubaev, E. V. Podryabinkin, G. L. Hart, and A. V. Shapeev, Accelerating high-throughput searches for new alloys with active learning of interatomic potentials, *Comput. Mater. Sci.* **156**, 148 (2019).

[13] R. Wang, W. Xia, T. J. Slade, X. Fan, H. Dong, K.-M. Ho, P. C. Canfield, and C.-Z. Wang, Machine learning guided discovery of ternary compounds involving La and immiscible Co and Pb elements, *npj Comp. Mater.* **8**, 258 (2022).

[14] M. Minotakis, H. Rossignol, M. Cobelli, and S. Sanvito, Machine-learning surrogate model for accelerating the search of stable ternary alloys, *Phys. Rev. Mater.* **7**, 093802 (2023).

[15] J. Roberts, B. Rijal, S. Divilov, J.-P. Maria, W. G. Fahrenholtz, D. E. Wolfe, D. W. Brenner, S. Curtarolo, and E. Zurek, Machine Learned Interatomic Potentials for Ternary Carbides trained on the AFLOW Database, arXiv: , 2401.01852v1 (2024).

[16] H. Rossignol, M. Minotakis, M. Cobelli, and S. Sanvito, Machine-Learning-Assisted Construction of Ternary Convex Hull Diagrams, *J. Chem. Inf. Model.* , in press (2024).

[17] J. Nelson and S. Sanvito, Predicting the curie temperature of ferromagnets using machine learning, *Phys. Rev. Mater.* **3**, 104405 (2019).

[18] G. R. Schleider, B. Focassio, and A. Fazzio, Machine learning for materials discovery: Two-dimensional topological insulators, *Appl. Phys. Rev.* **8**, 031409 (2021).

[19] M. Cobelli, P. Cahalane, and S. Sanvito, Local inversion of the chemical environment representations, *Phys. Rev. B* **106**, 035402 (2022).

[20] F. Zipoli, V. Viterbo, O. Schilter, L. Kahle, and T. Laino, Prediction of Phase Diagrams and Associated Phase Structural Properties, *Ind. Eng. Chem. Res.* **61**, 8378 (2022).

[21] R. Pederson, B. Kalita, and K. Burke, Machine learning and density functional theory, *Nature Rev. Phys.* **4**, 357 (2022).

[22] F. Brockherde, L. Vogt, L. Li, M. E. Tuckerman, K. Burke, and K.-R. Müller, Bypassing the Kohn-Sham equations with machine learning, *Nature Commun.* **8**, 872 (2017).

[23] R. Nagai, R. Akashi, and O. Sugino, Completing density functional theory by machine learning hidden messages from molecules, *npj Comput. Mater.* **6**, 43 (2020).

[24] L. Li, S. Hoyer, R. Pederson, R. Sun, E. D. Cubuk, P. Riley, and K. Burke, Kohn-Sham Equations as Regularizer: Building Prior Knowledge into Machine-Learned Physics, *Phys. Rev. Lett.* **126**, 036401 (2021).

[25] J. Kirkpatrick, B. McMorrow, D. H. P. Turban, A. L. Gaunt, J. S. Spencer, A. G. D. G. Matthews, A. Obika, L. Thiry, M. Fortunato, D. Pfau, L. R. Castellanos, S. Petersen, A. W. R. Nelson, P. Kohli, P. Mori-Sánchez, D. Hassabis, and A. J. Cohen, Pushing the frontiers of density functionals by solving the fractional electron problem, *Science* **374**, 1385 (2021).

[26] J. Nelson, R. Tiwari, and S. Sanvito, Machine learning density functional theory for the Hubbard model, *Phys. Rev. B* **99**, 075132 (2019).

[27] K. Ryczko, D. A. Strubbe, and I. Tamblyn, Deep learning and density-functional theory, *Phys. Rev. A* **100**, 022512 (2019).

[28] E. V. Boström, P. Helmer, P. Werner, and C. Verdozzi, Electron-electron versus electron-phonon interactions in lattice models: Screening effects described by a density functional theory approach, *Phys. Rev. Res.* **1**, 013017 (2019).

[29] J. R. Moreno, G. Carleo, and A. Georges, Deep learning the hohenberg-kohn maps of density functional theory, *Phys. Rev. Lett.* **125**, 076402 (2020).

[30] A. Grisafi, A. Fabrizio, B. Meyer, D. M. Wilkins, C. Corminboeuf, and M. Ceriotti, Transferable machine-learning model of the electron density, *ACS Cent. Sci.* **5**, 57 (2019).

[31] A. M. Lewis, A. Grisafi, M. Ceriotti, and M. Rossi, Learning Electron Densities in the Condensed Phase, *J. Chem. Theory Comput.* **17**, 7203 (2021).

[32] L. Zepeda-Núñez, Y. Chen, J. Zhang, W. Jia, L. Zhang, and L. Lin, Deep Density: Circumventing the Kohn-Sham equations via symmetry preserving neural networks, *J. Comp. Phys.* **443**, 110523 (2021).

[33] J. A. Rackers, L. Tecot, M. Geiger, and T. E. Smidt, A recipe for cracking the quantum scaling limit with machine learned electron densities, *Mach. Learn.: Sci. Technol.* **4**, 015027 (2023).

[34] A. Chandrasekaran, D. Kamal, R. Batra, C. Kim, L. Chen, and R. Ramprasad, Solving the electronic structure problem with machine learning, *npj Comput. Mater.* **5**, 22 (2019).

[35] J. A. Ellis, L. Fiedler, G. A. Popoola, N. A. Modine, J. A. Stephens, A. P. Thompson, A. Cangi, and S. Rajamanickam, Accelerating finite-temperature Kohn-Sham density functional theory with deep neural networks, *Phys. Rev. B* **104**, 035120 (2021).

[36] T. Lv, Z. Zhong, Y. Liang, F. Li, J. Huang, and R. Zheng, Deep charge: Deep learning model of electron density from a one-shot density functional theory calculation, *Phys. Rev. B* **108**, 235159 (2023).

[37] B. Focassio, M. Domina, U. Patil, A. Fazzio, and S. Sanvito, Linear Jacobi-Legendre expansion of the charge density for machine learning-accelerated electronic structure calculations, *npj Comput. Mat.* **23**, 01053 (2023).

[38] E. M. Sunshine, M. Shuaibi, Z. W. Ulissi, and J. R. Kitchin, Deep charge: Deep learning model of electron density from a one-shot density functional theory calculation, *J. Phys. Chem. C* **127**, 23459 (2023).

[39] A. Grisafi, A. Bussy, M. Salanne, and R. Vuilleumier, Predicting the charge density response in metal electrodes, *Phys. Rev. Mater.* **7**, 125403 (2023).

[40] B. G. del Rio, B. Phan, and R. Ramprasad, A deep learning framework to emulate density functional theory, *npj Comp. Mater.* **9**, 158 (2023).

[41] M. Domina, U. Patil, M. Cobelli, and S. Sanvito, Cluster expansion constructed over jacobi-legendre polynomials for accurate force fields, *Phys. Rev. B* **108**, 094102 (2023).

[42] G. Kresse and J. Furthmüller, Efficient iterative schemes for ab initio total-energy calculations using a plane-wave basis set, *Phys. Rev. B* **54**, 11169 (1996).

[43] G. Kresse and J. Furthmüller, Efficiency of ab-initio total energy calculations for metals and semiconductors using a plane-wave basis set, *Comput. Mater. Sci.* **6**, 15 (1996).

[44] P. E. Blöchl, Projector augmented-wave method, *Phys. Rev. B* **50**, 17953 (1994).

[45] G. Kresse and D. Joubert, From ultrasoft pseudopotentials to the projector augmented-wave method, *Phys. Rev. B* **59**, 1758 (1999).

[46] P. Giannozzi, S. Baroni, N. Bonini, M. Calandra, R. Car, C. Cavazzoni, D. Ceresoli, G. L. Chiarotti, M. Cococcioni, I. Dabo, A. D. Corso, S. de Gironcoli, S. Fabris, G. Fratesi, R. Gebauer, U. Gerstmann, C. Gougauss, A. Kokalj, M. Lazzeri, L. Martin-Samos, N. Marzari, F. Mauri, R. Mazzarello, S. Paolini, A. Pasquarello, L. Paulatto, C. Sbraccia, S. Scandolo, G. Scaluzero, A. P. Seitsonen, A. Smogunov, P. Umari, and R. M. Wentzcovitch, QUANTUM ESPRESSO: a modular and open-source software project for quantum simulations of materials, *J. Phys.: Condens. Matter* **21**, 395502 (2009).

[47] P. Giannozzi, O. Andreussi, T. Brumme, O. Bunau, M. B. Nardelli, M. Calandra, R. Car, C. Cavazzoni, D. Ceresoli, M. Cococcioni, N. Colonna, I. Carnimeo, A. D. Corso, S. de Gironcoli, P. Delugas, R. A. DiStasio, A. Ferretti, A. Floris, G. Fratesi, G. Fugallo, R. Gebauer, U. Gerstmann, F. Giustino, T. Gorni, J. Jia, M. Kawamura, H.-Y. Ko, A. Kokalj, E. Küçükbenli, M. Lazzeri, M. Marsili, N. Marzari, F. Mauri, N. L. Nguyen, H.-V. Nguyen, A. O. de-la Roza, L. Paulatto, S. Poncée, D. Rocca, R. Sabatini, B. Santra, M. Schlipf, A. P. Seitsonen, A. Smogunov, I. Timrov, T. Thonhauser, P. Umari, N. Vast, X. Wu, and S. Baroni, Advanced capabilities for materials modelling with Quantum ESPRESSO, *J. Phys.: Condens. Matter* **29**, 465901 (2017).

[48] J. J. Mortensen, L. B. Hansen, and K. W. Jacobsen, Real-space grid implementation of the projector augmented wave method, *Phys. Rev. B* **71**, 035109 (2005).

[49] X. Gonze, B. Amadon, G. Antonius, F. Arnardi, L. Baguet, J.-M. Beuken, J. Bieder, F. Bottin, J. Bouchet, E. Bousquet, N. Brouwer, F. Bruneval, G. Brunin, T. Cavignac, J.-B. Charraud, W. Chen, M. Côté, S. Cottenier, J. Denier, G. Geneste, P. Ghosez, M. Giantomassi, Y. Gillet, O. Gingras, D. R. Hamann, G. Hautier, X. He, N. Helbig, N. Holzwarth, Y. Jia, F. Jollet, W. Lafargue-Dit-Hauret, K. Lejaeghere, M. A. Marques, A. Martin, C. Martins, H. P. Miranda, F. Naccarato, K. Persson, G. Petretto, V. Planes, Y. Pouillon, S. Prokhorenko, F. Ricci, G.-M. Rignanese, A. H. Romero, M. M. Schmitt, M. Torrent, M. J. van Setten, B. Van Troeye, M. J. Verstraete, G. Zérah, and J. W. Zwanziger, The abinit project: Impact, environment and recent developments, *Comput. Phys. Commun.* **248**, 107042 (2020).

[50] H. Jónsson, G. Mills, and K. W. Jacobsen, Nudged elastic band method for finding minimum energy paths of transitions, in *Classical and Quantum Dynamics in Condensed Phase Simulations*, pp. 385–404.

[51] G. Henkelman and H. Jónsson, Improved tangent estimate in the nudged elastic band method for finding minimum energy paths and saddle points, *J. Chem. Phys.* **113**, 9978 (2000).

[52] G. Henkelman, B. P. Uberuaga, and H. Jónsson, A climbing image nudged elastic band method for finding saddle points and minimum energy paths, *J. Chem. Phys.* **113**, 9901 (2000).

[53] A. H. Larsen, J. J. Mortensen, J. Blomqvist, I. E. Castelli, R. Christensen, M. Dułak, J. Friis, M. N. Groves, B. Hammer, C. Hargus, E. D. Hermes, P. C. Jennings, P. B. Jensen, J. Kermode, J. R. Kitchin, E. L. Kolsbørg, J. Kubal, K. Kaasbørg, S. Lysgaard, J. B. Maronsson, T. Maxson, T. Olsen, L. Pastewka, A. Petersen, C. Rostgaard, J. Schiøtz, O. Schütt, M. Strange, K. S. Thygesen, T. Vegge, L. Vilhelmsen, M. Walter, Z. Zeng, and K. W. Jacobsen, The atomic simulation environment-a python library for working with atoms, *J. Phys.: Condens. Matter* **29**, 273002 (2017).

[54] J. P. Perdew, J. A. Chevary, S. H. Vosko, K. A. Jackson, M. R. Pederson, D. J. Singh, and C. Fiolhais, Atoms, molecules, solids, and surfaces: Applications of the generalized gradient approximation for exchange and correlation, *Phys. Rev. B* **46**, 6671 (1992).

[55] J. P. Perdew, K. Burke, and M. Ernzerhof, Generalized gradient approximation made simple, *Phys. Rev. Lett.* **77**, 3865 (1996).

[56] S. Nosé, A unified formulation of the constant temperature molecular dynamics methods, *J. Chem. Phys.* **81**, 511 (1984).

[57] S. Nosé, A molecular dynamics method for simulations in the canonical ensemble, *Mol. Phys.* **100**, 191 (1984).

[58] W. G. Hoover, Canonical dynamics: Equilibrium phase-space distributions, *Phys. Rev. A* **31**, 1695 (1985).

[59] S. P. Ong, W. D. Richards, A. Jain, G. Hautier, M. Kocher, S. Cholia, D. Gunter, V. Chevrier, K. A. Persson, and G. Ceder, Python Materials Genomics (pymatgen) : A Robust, Open-Source Python Library for Materials Analysis, *Comput. Mater. Sci.* **68**, 314 (2013).

[60] F. Pedregosa, G. Varoquaux, A. Gramfort, V. Michel, B. Thirion, O. Grisel, M. Blondel, P. Prettenhofer, R. Weiss, V. Dubourg, J. Vanderplas, A. Passos, D. Cournapeau, M. Brucher, M. Perrot, and E. Duchesnay, Scikit-learn: Machine learning in Python, *J. Mach. Learn. Res.* **12**, 2825 (2011).

[61] T. Head, M. Kumar, H. Nahrstaedt, G. Louppe, and I. Shcherbatyi, *scikit-optimize* (2021).

[62] B. Focassio, M. Domina, U. Patil, A. Fazzio, and S. Sanvito, Dataset and models from: Covariant Jacobi-Legendre expansion for total energy calculations within the projector-augmented-wave formalism (2024).